ENGINEERING

Multiscale crack trapping for programmable adhesives

Seongjin Park[1]†, Dong Kwan Kang[1]†, Donghyuk Lee[1]†, Geonjun Choi[1], Jaeil Kim[1], Chanhong Lee[2], Minho Seong[1], Michael D. Bartlett[2,3]*, Hoon Eui Jeong[1]*

The precise control of crack propagation at bonded interfaces is crucial for smart adhesives with advanced performance. However, previous studies have primarily concentrated on either microscale or macroscale crack propagation. Here, we present a hybrid adhesive that integrates microarchitectures and macroscopic nonlinear cut architectures for unparalleled adhesion control. The integration of these architectural elements enables conformal attachment and simultaneous crack trapping across multiple scales for high capacity, enhancing adhesion by more than 70×, while facilitating crack propagation at the macroscale in specific directions for programmable release and reusability. As adhesion strength and directionality can be independently controlled at any location, skin adhesive patches are created that are breathable, nondamaging, and exceptionally strong and secure yet remove easily. These capabilities are demonstrated with a skin-mounted adhesive patch with integrated electronics that accurately detects human motion and wirelessly transmits signals, enabling real-time control of avatars in virtual reality applications.

INTRODUCTION

Strong yet reversible interfacial adhesion is crucial for a range of emerging applications, including wearable devices (*1*, *2*), soft robotics (*3*–*5*), and pick-and-place manufacturing (*6*, *7*). These domains increasingly demand advanced adhesive technologies with specific attributes, such as robust and tunable adhesion strength, switchable and directional adhesion, high reusability, and minimal surface damage or contamination (*8*–*10*). This is particularly vital for wearable devices, where establishing robust, intimate, and reversible adhesion to the skin without causing any skin damage is essential (*11*, *12*). Furthermore, factors such as breathability and biocompatibility are essential for skin adhesion (*13*). Conventional adhesives, such as pressure-sensitive adhesives and tacky hydrogels, have been widely used in wearable technologies because of their ease of application (*14*–*16*). These materials primarily focus on modulating surface chemistry and dissipating mechanical energy to mitigate crack initiation and propagation, thereby achieving high adhesion strength. However, as dissipative or chemical mechanisms often act the same in all directions, release can become more difficult and reduce adhesion directionality. Therefore, these types of systems have moved to using various stimuli to aid in release, which has proven effective in controlled environments (*17*, *18*). Going forward, passive approaches where release mechanisms are built into the structure of the adhesive, rather than into a specific stimulus, offer the possibility of functioning in a broader range of conditions where the environment or use case may be variable or difficult to control (*19*). These challenges underscore the pressing need for a wider selection of advanced adhesive solutions (*20*, *21*).

The adhesion properties of materials are fundamentally governed by the mechanics of crack propagation occurring at bonded interfaces. Therefore, the evolution of smart adhesives with enhanced capabilities requires refined control over crack propagation behavior within these interfaces (*22*–*25*). Nature offers a remarkable strategy for achieving this through the intricate control of interfacial crack propagation through heterogeneous structures. For instance, at the microscopic scale, the foot hairs found in geckos or beetles effectively trap cracks at each discrete microhair, necessitating the reinitiation of crack for further peeling progress (*26*–*28*). These microscale foot hairs also maximize interfacial contact area and enhance van der Waals interactions against diverse surfaces. Biomimetic adhesives adopting this microscale crack-trapping strategy enable robust adhesion yet easy release across a range of surfaces (*29*, *30*). At the macroscale, organisms like the barnacle use the stiffness and geometry of its shell and base plate to trap cracks for strong attachment (*31*). Synthetic adhesives have leveraged similar strategies to control cracks at the macroscale through passive and active control of stiffness (*32*–*34*) or by material patterning through features such as incisions or discontinuities (*35*–*37*). For example, kirigami-inspired adhesives, or metamaterial adhesives, integrate deliberate macroscopic cuts into thin adhesive films. By introducing macroscale nonlinear cuts in metamaterial adhesive films, cracks can be trapped and even reverses crack propagation direction in a variety of adhesive materials (*38*–*40*). These various studies demonstrate how precise control over the movement of cracks across a bonded interface can lead to the development of advanced smart adhesion properties. While considerable strides have been made in understanding the mechanisms of crack and fracture dynamics in adhesion science, previous studies have primarily focused on crack trapping at either the microscale or the macroscale. Functioning across multiple scales will be critical to reliable attachment on irregular surfaces such as skin, where small scale roughness provides a barrier to robust attachment. Bridging the gap between these two divergent length scales holds immense potential to establish a new milestone in adhesion and fracture dynamics. However, despite extensive investigations into reversible smart adhesives, multiscale mechanisms for controlling crack dynamics remain underexplored.

Herein, we present a strategy that controls crack propagation across multiple length scales to create advanced functional adhesives. This approach uses microscale crack-trapping mechanisms through pillar microarchitectures and macroscale crack-trapping mechanisms using nonlinear cut macroarchitectures within a single

[1]Department of Mechanical Engineering, Ulsan National Institute of Science and Technology (UNIST), Ulsan 44919, Republic of Korea. [2]Department of Mechanical Engineering, Soft Materials and Structures Lab, Virginia Tech, Blacksburg, VA, USA. [3]Macromolecules Innovation Institute, Virginia Tech, Blacksburg, VA, USA.
*Corresponding author. Email: hoonejeong@unist.ac.kr (H.E.J.); mbartlett@vt.edu (M.D.B.)
†These authors contributed equally to this work.

adhesive film. This multiscale crack-trapping mechanism enables the programming of multiple adhesion characteristics by synergizing the major advantages of microscale and macroscale crack control strategies. This enables the control of crack initiation at small scales to improve contact and energy dissipation while programming crack propagation direction and trapping behaviors at the macroscale. This approach creates an adhesive film that continuously initiates and traps cracks at multiple scales for high capacity while facilitating continuous crack propagation at the macroscale in specific directions for substantial and programmable adhesion anisotropy. This enables notably strong adhesion in both normal and peeling conditions, high directionality, adaptability to rough surfaces, and reliable reusability. In quantitative adhesion assessments, the crack-arresting hybrid adhesive demonstrates outstanding pull-off and peel adhesion simultaneously, with a pull-off strength of 272.7 kPa and peel adhesion capacity of 220.4 N m^{-1}. These values represent 1.9× and 73.9× improvements, respectively, compared to planar adhesives made from the same materials. Notably, the hybrid adhesive exhibits reusability (over 50 cycles) and excellent adhesion directionality, reaching a maximum value over 20, while also showing high adhesion strength. This provides exceptional combinations of high strength and directionality for high-capacity and easy-release skin adhesives, showing exceptional performance as compared to previous literature results. As adhesion strength and directionality are independently controlled at any location on the adhesive, skin adhesive patches are created that are breathable, nondamaging, and exceptionally strong and secure yet remove easily. By integrating electronic devices such as a gyroscope sensor, Bluetooth module, and battery, our crack-arresting hybrid patch securely adheres to skin surfaces while wirelessly detecting the wearer's dynamic movements. The remarkable adhesion capability of the hybrid adhesive based on a multiscale crack-trapping mechanism not only contributes to adhesion science but also has practical applications in diverse emerging fields.

RESULTS

Design and working principle of the crack-trapping hybrid adhesive

Figure 1A illustrates the design of the crack-trapping hybrid adhesive patch, fabricated using polydimethylsiloxane (PDMS). PDMS is a biocompatible material and thus suitable for skin-interfaced and wearable applications (*41*, *42*). This patch uses microscale pillar arrays with macroscale nonlinear cuts to maximize the crack-trapping effect across length scales. The microscale pillars, featuring hexagonal cross sections and mushroom-shaped tips, greatly enhance interfacial adhesion. Acting as barriers at the microscopic level, these pillars effectively impede crack propagation commonly seen in conventional flat adhesive interfaces. Their discrete structure forces crack reinitiation at each subsequent micropillar, and their mushroom-shaped tips distribute stress more uniformly, notably improving adhesion (Fig. 1A) (*43*–*45*). Moreover, these micropillars exhibit superior adaptability to rough surfaces and increased tolerance to contaminants compared to flat PDMS surfaces. Arranged in a hexagonal array, these microstructures maximize packing density within a given area, leading to amplified interfacial contact area and improved adhesion (Fig. 1A).

At the macroscopic level, the open rectangular cuts play a pivotal role in promoting interfacial peeling adhesion by controlling the direction of crack propagation (Fig. 1B). When peeling the hybrid adhesive patch in the maximum force direction, cracks propagate until they encounter the interconnect tip located at the base of the rectangular cut (Fig. 1Bi) (*38*). Upon reaching these tips, the crack is arrested and subsequently reverses its propagation until complete delamination of the patch occurs (Fig. 1Bii). During the reverse crack propagation in the maximum force direction, the cuts induce a transformation of a high global peel angle (θ) into a lower local peel angle (θ_α) at the adhesive interfaces (Fig. 1Biii). It is important to note that, alongside the rectangular cuts, the micropillars play a notable role in boosting peeling capacity at the microscale. They delay crack propagation in both the maximum force and minimum force peeling directions and enhance crack entrapment at the interconnect tips. Exploiting these remarkable adhesion capabilities, the hybrid patch can evolve into a versatile, flexible, and wearable sensor platform by integrating nanomaterials-based sensors or commercial sensors onto it (Fig. 1A).

Hybrid adhesive patch fabrication and geometry

Figure 2A illustrates a schematic depicting the fabrication process of the hybrid adhesive patch (see also fig. S1). Initially, a master mold for a hexagonal micropillar array with protruding tips was prepared through photolithography process (Fig. 2Ai and fig. S1). Subsequently, PDMS was poured and spin coated on the master mold and baked (thickness, 75 μm; 1:20 curing agent) (Fig. 2Aii; for more details, please refer to Materials and Methods). A polyethylene terephthalate (PET) film with a thin PDMS layer (PET thickness, 50 μm; spin-coated PDMS thickness, 75 μm) served as the inextensible backing layer. It is important to note that if the PET backing layer is too thick (e.g., > 100 μm), it can reduce the patch's conformability, thereby deteriorating its skin adhesion capacity. The PDMS side of the PET backing film was then bonded to the rear side of the hexagonal micropillar array using O_2 plasma–assisted bonding (Fig. 2Aiii), followed by demolding (Fig. 2Aiv). Subsequently, open rectangular cuts were inscribed into the assembled film, resulting in the creation of a micropillar-nonlinear cut hybrid adhesive patch (Fig. 2Av). When applicable, sensors or other devices were integrated into the patch for various applications (Fig. 2Avi).

Figure 2B presents a photograph and scanning electron microscopy (SEM) images of the fabricated patch and its surface microstructures. These microstructures, characterized by hexagonal cross sections, are arranged in a hexagonal array to maximize the interfacial contact area, thereby enhancing adhesion strength. During the photoresist developing process in the master mold fabrication, the corners of the hexagonal microstructures were slightly rounded. The microstructures have specific dimensions: a stem diameter of 20 μm, a tip diameter of 28 μm, a tip thickness of 2 to 3 μm, and a height of 15 μm. The height was chosen to prevent structural collapse. When the height exceeded 30 μm, the micropillars began to exhibit lateral collapse. The pillar spacing ratio (PSR = interspacing between micropillars / stem diameter of micropillars) of this array varied from 0.5 to 3 (fig. S2). However, in our primary tests, we predominantly used micropillar arrays with a PSR of 0.5 as the sample with 0.5 PSR exhibited the highest pull-off strength while maintaining structural integrity (note S1 and fig. S3).

In designing nonlinear cuts, we prepared four distinct rectangular cuts based on the concept of a critical length (l_{ch}; Fig. 2C). When the critical length (l_{ch}) is smaller than half of the rectangular cut width (w_p) (i.e., $l_{ch} < 0.5w_p$), cracks originating at each tip of interconnects do not overlap (Fig. 2C). This leads to circular delaminated regions

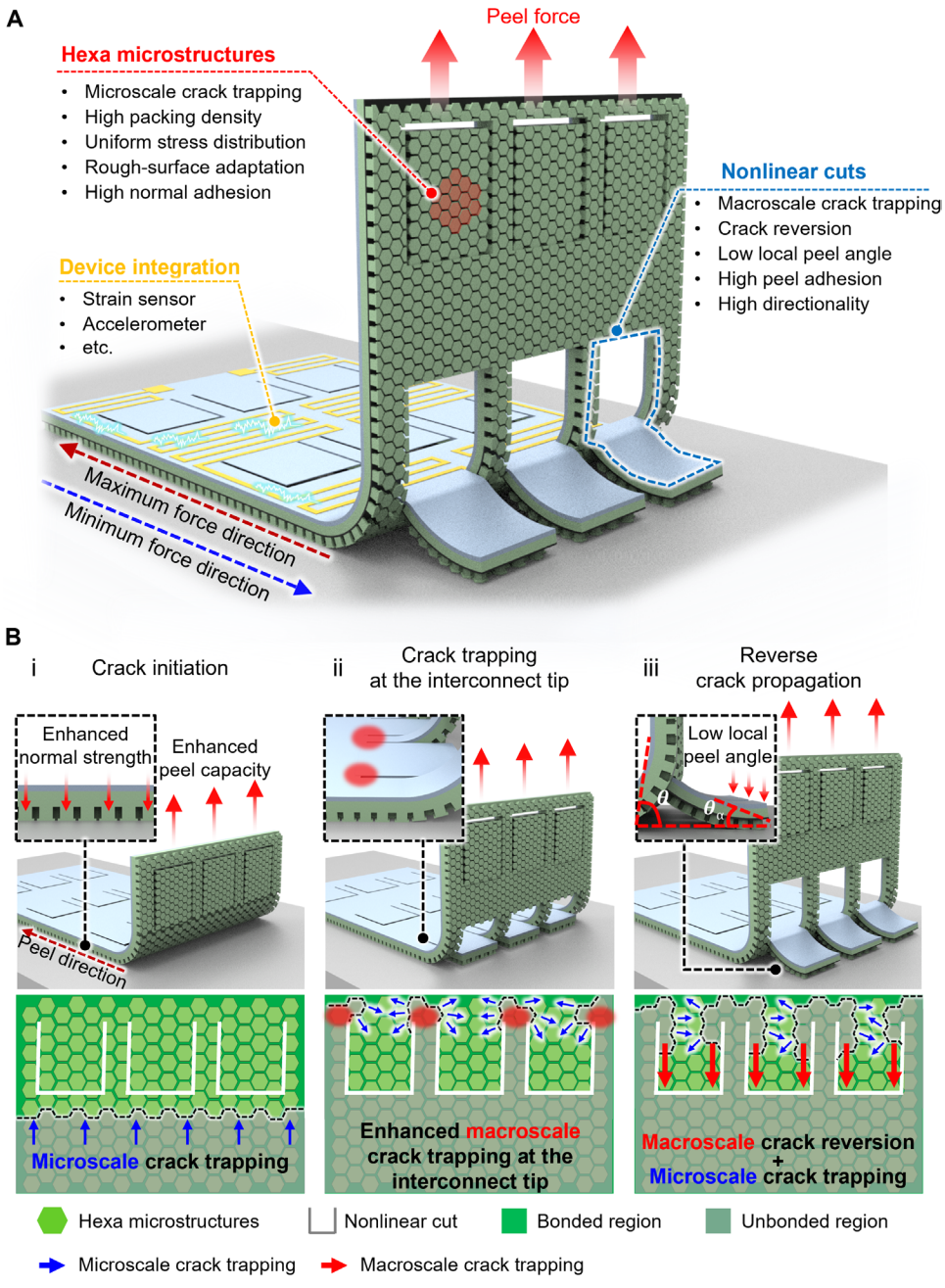

Fig. 1. Design of crack-trapping hybrid adhesive patch. (**A**) The patch incorporates hexagonal micropillars, nonlinear cuts, and sensors into a thin film configuration. (**B**) Crack propagation mechanisms in the hybrid adhesive patch during peeling. (i) Angled view (top) and top view (bottom) of the hybrid patch depicting the crack initiation step during the maximum force directional peeling process. (ii) Angled view (top) and top view (bottom) of the hybrid patch illustrating the crack-trapping step during the maximum force directional peeling process. (iii) Angled view (top) and top view (bottom) of the hybrid patch showing the crack reversion step during the maximum force directional peeling process.

centered at each interconnect, maximizing the crack-trapping effect introduced by the rectangular cut. Conversely, when l_{ch} is larger than $0.5w_p$, cracks from adjacent interconnect tips merge before reaching the maximum peeling force. The critical length, l_{ch} is determined using the following Eq. 1 (*38*)

$$l_{ch} = \sqrt{\frac{2D}{G_c}\frac{w_{int}}{w}\left(N_p^* + 1\right)} \quad (1)$$

Here, D represents the flexural rigidity of the adhesive film, G_c is the critical energy release rate or adhesion energy, w_{int} is the width of the interconnect, w is the total width, and N_p^* is the optimal number of cuts (Fig. 2Ci). According to this equation, l_{ch} is calculated to be 2.1 mm for the planar PDMS film and 1.3 mm for the microstructured film. The variation in l_{ch} between the planar and micropillar samples can be attributed to the different G_c values, where the adhesion energy for the planar PDMS (G_c) is 3.0 N m^{-1}, and the adhesion

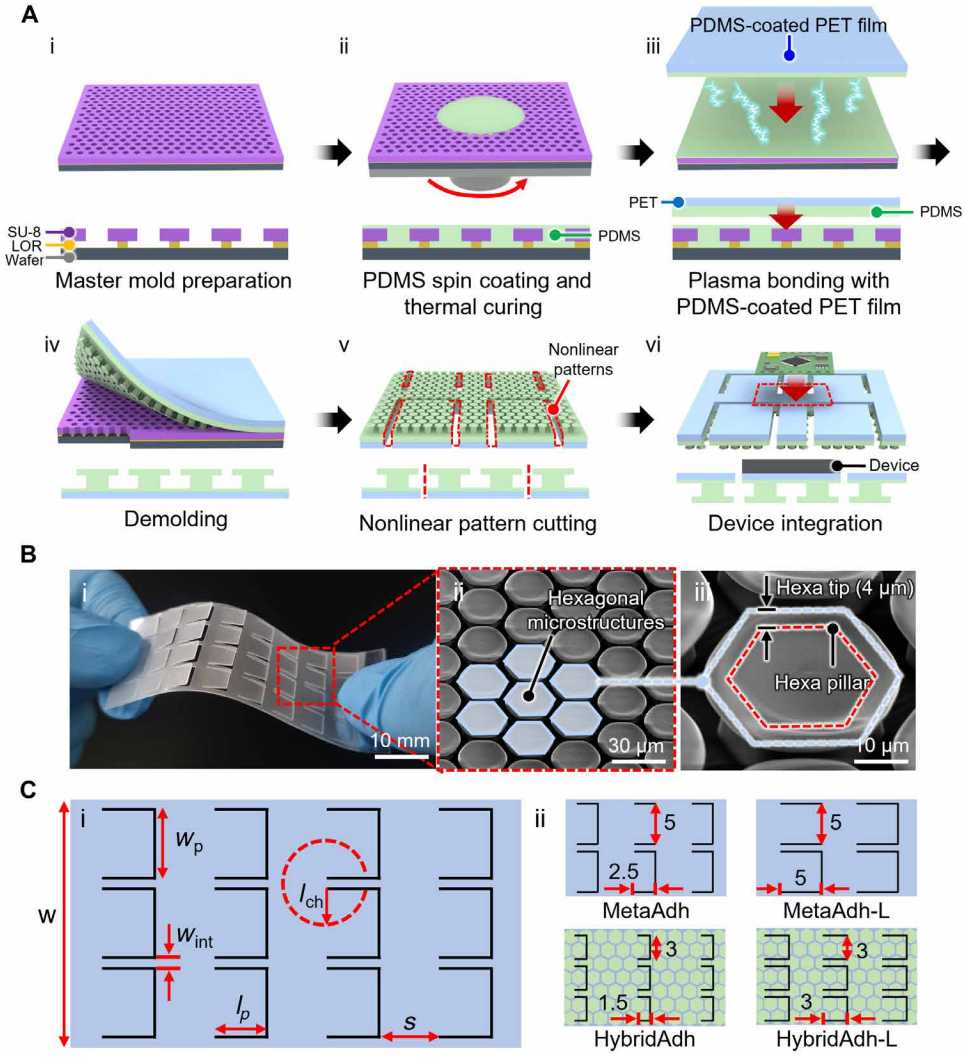

Fig. 2. Fabrication of crack-trapping hybrid adhesive patch. (**A**) Detailed fabrication procedure for the crack-trapping hybrid adhesive patch. (**B**) (i) Photograph displaying the fabricated hybrid adhesive patch, (ii) SEM images of the fabricated hexagonal micropillar array, and (iii) an enlarged view of the micropillar array. (**C**) (i) Design and geometrical parameters of the hybrid adhesive patch. (ii) Design and sizes of different hybrid adhesive patches: MetaAdh, MetaAdh-L, HybridAdh, and HybridAdh-L.

energy for the microstructured PDMS ($G_{c,p}$) is 10.8 N m^{-1}. Consequently, we set the width (w_p) of a single cut, which is 2*l_{ch}, to 5 mm for the flat PDMS film (referred to as "MetaAdh") and 3 mm for the hybrid sample (referred to as "HybridAdh"). The vertical length (l_p) of a single cut and the height of the interconnect (s) were prepared to be either as l_{ch} or 2*l_{ch}. Samples with the longer l_p (2*l_{ch}) were denoted as "MetaAdh-L" or "HybridAdh-L" (Fig. 2Cii). w_{int} was set to 1 mm for MetaAdh and 2 mm for HybridAdh (table S2).

Adhesion performance of the hybrid adhesive patch

To investigate the impact of hexagonal micropillars and nonlinear cuts on adhesive performance, we evaluated the peeling behavior of various adhesive films against a flat glass through a 90° peel test at a retraction rate of 1 mm s^{-1} (Fig. 3A and fig. S4). The tests were conducted in both maximum peeling force and minimum peeling force directions (Fig. 3, B and C). The hexagonal micropillars (denoted as "MicroAdh") on the continuous backing layer exhibited a notably improved adhesion strength of 10.8 N m^{-1} on glass, compared to the adhesion strength of 3.0 N m^{-1} observed with planar PDMS. This improvement can be attributed to the discrete nature of individual micropillars, which necessitate the reinitiation of the crack during the peeling process. In contrast, with the planar film, once a crack initiates propagation, the interface separates completely without any crack arrest or delay, resulting in a lower peel force. Nonetheless, the adhesion strength of MicroAdh was much lower than that of commercial Scotch tape (35.1 N m^{-1}).

Notably, the metamaterial adhesive samples displayed even higher adhesion strength compared to the MicroAdh or Scotch tape. For instance, the MetaAdh sample exhibited an impressive adhesion strength of 63.0 N m^{-1} in the maximum force direction. This represents 21.1×, 5.8×, and 1.8× increases over the values obtained for the planar PDMS, MicroAdh, and Scotch tape, respectively. This substantial improvement can be attributed to the metamaterial adhesive cut's ability to trap at the tips of interconnects and reverse propagating cracks when subjected to further loading in the maximum force peeling direction. This action effectively delays overall

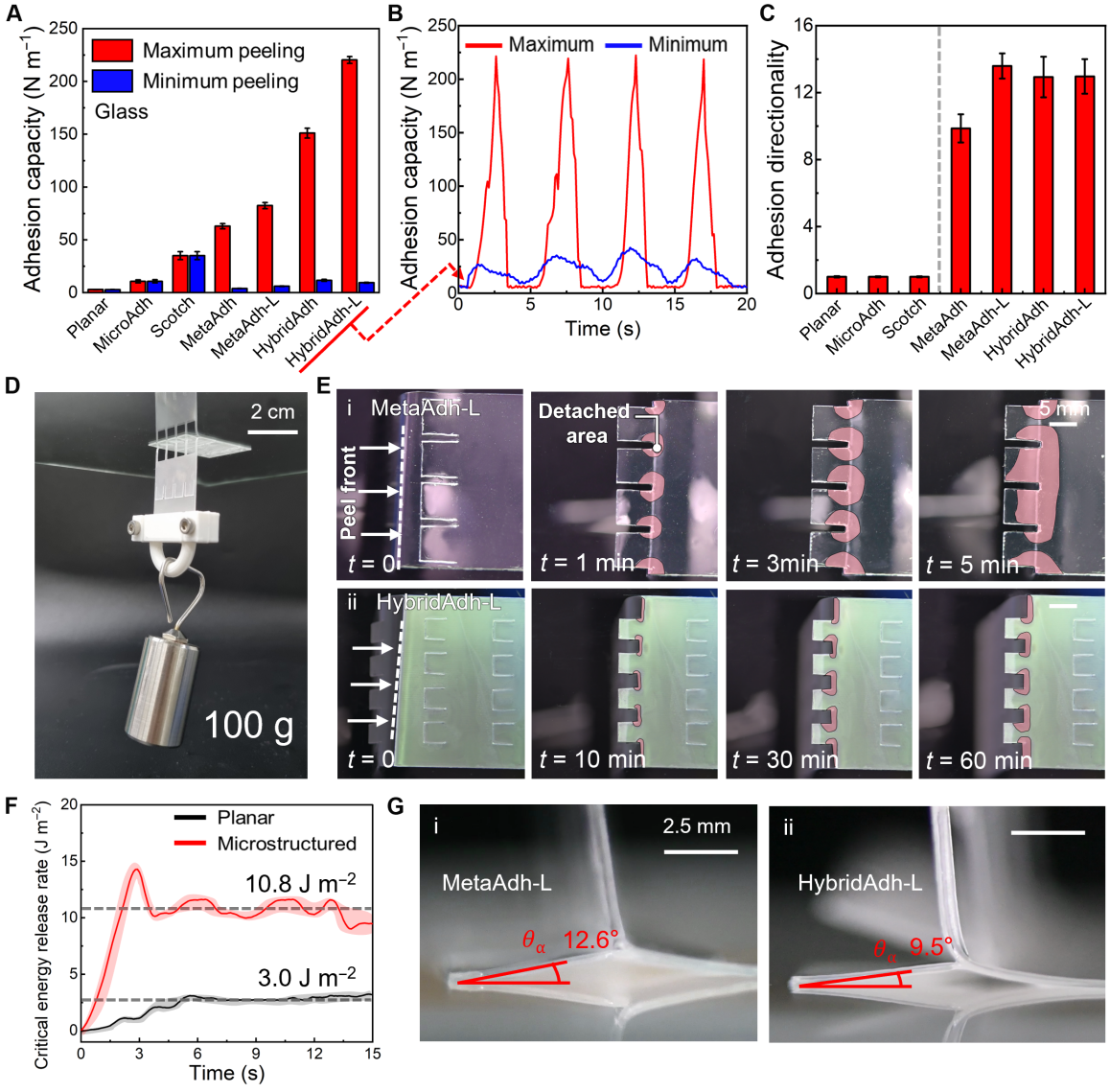

Fig. 3. Adhesion performance of the hybrid adhesive patch. (**A**) Adhesion strengths measured for various adhesive samples against a glass substrate in both maximum force and minimum force directions (retraction rate, 1 mm s^{-1}). (**B**) Adhesion strengths of the hybridAdh-L sample in the maximum force and minimum force directions during repeated test cycles. (**C**) Adhesion directionality (F_{max}/F_{min}) of different adhesive samples on a glass substrate. (**D**) Photograph demonstrating the robust adhesion of the hybrid adhesive (HybridAdh-L) to glass during maximum force directional peeling with a 100-g weight. (**E**) Time-lapse photographs illustrating the peeling process of the (i) MetaAdh-L sample and (ii) HybridAdh-L sample attached to glass during maximum force directional peeling with a 100-g weight. False color added to enhance contrast. (**F**) Critical energy release rate comparison between planar PDMS and microstructured PDMS (retraction rate, 1 mm s^{-1}). (**G**) Photographs displaying the side view and local peel angle (θ_α) of the (i) MetaAdh-L sample and (ii) Hybrid-L sample adhered to glass during a 90° peel test.

crack propagation. Moreover, the metamaterial adhesive transforms a high global peel angle into a lower local peel angle, further contributing to enhanced adhesion strength (Fig. 1B). According to an adhesive peel model, a lower peeling angle can substantially enhance adhesion strength (*46*, *47*)

$$\frac{F_c}{w} = \frac{G_c}{1 - \cos\theta} \quad (2)$$

Here, F_c represents the peel force at an angle θ from a substrate, w is the film width, and G_c is the adhesion energy. This indicates that the adhesion strength is directly proportional to the adhesion energy and inversely proportional to the peeling angle. The cut length (l_p) of the metamaterial adhesive also had a noticeable impact on peel strength. The MetaAdh-L sample exhibited superior adhesion strengths of 82.4 N m^{-1} compared to the MetaAdh sample (63.0 N m^{-1}). This improvement can be attributed to the longer cuts' ability to induce smaller local peel angles and reverse crack propagation over a greater distance and duration.

When hexagonal micropillars were integrated into the metamaterial adhesive film, the resulting hybrid film exhibited greatly enhanced adhesion strength. For instance, the HybridAdh sample demonstrated an adhesion strength of 151.1 N m^{-1}, while the HybridAdh-L

exhibited an even higher adhesion strength at 220.4 N m^{-1} (Fig. 3A). Notably, the adhesion strength of 220.4 N m^{-1} achieved with the HybridAdh-L represented a remarkable increase, surpassing values obtained with flat PDMS (3.0 N m^{-1}), MicroAdh (10.8 N m^{-1}), and simple MetaAdh (63.0 N m^{-1}) by 73.5×, 20.4×, and 3.5×, respectively. These results emphasize the synergistic enhancement of peel adhesion performance achieved through the integration of micropillar arrays and nonlinear cuts, allowing for crack trapping at both the microscale and macroscale levels. We observed that the hybrid adhesive, when subjected to 100-g weight in the 90° direction, can better endure external loading for an extended period of time (>1 hour) than the simple metamaterial adhesive sample (MetaAdh-L) (Fig. 3, D and E). This is attributed to (i) the higher adhesion energy of micropillar arrays compared to a flat PDMS film and (ii) this higher adhesion energy driving a lower peel angle at the adhesive interface (Fig. 3, F and G).

Directional adhesion is a crucial feature of advanced adhesives, as it allows for strong adhesion in one direction while facilitating easy release in the opposite direction. This property enables a wide range of applications that require adhesion anisotropy. In the case of planar PDMS, MicroAdh, and Scotch tape, they did not exhibit any adhesion directionality, resulting in a directionality [adhesion in the maximum force direction (F_{max}) / adhesion in the minimum force direction (F_{min})] of 1 (Fig. 3C). In contrast, all nonlinear cuts-integrated samples, whether simple MetaAdh or HybridAdh, displayed noticeable adhesion directionality. For instance, MetaAdh-L, which demonstrated the highest peeling strength in the maximum force direction among the pure metamaterial adhesive samples, exhibited notable adhesion directionality with a ratio of 13.6. The adhesion strengths in the maximum force and minimum force directions were 82.4 and 6.1 N m^{-1}, respectively. This is because the anisotropic open rectangular cut design enables efficient crack trapping and reverse crack propagation in the maximum force peeling direction, resulting in increased adhesion strength, while crack propagation continues continuously at low adhesion strength in the minimum force direction (*48*). The remarkable directional attribute was also observed in the hexagonal micropillars-metamaterial adhesive hybrid samples. For example, the Hybrid-L displayed a substantial directional ratio of 13.0. These findings indicate that the hybrid samples can simultaneously exhibit multiple remarkable characteristics, including substantial pull-off strength, high peel capacity, and adhesion directionality (Fig. 1). Such multifaceted performance attributes have not been observed in previous adhesives.

Adhesion performance on rough surfaces

We also assessed the peeling performance of various adhesive films on porcine skin with microscale surface roughness (rms roughness, 12.2 μm) (Fig. 4, A and B, and fig. S5). The MicroAdh exhibited an adhesion strength of 4.5 N m^{-1}, marking a 2.4× enhancement compared to the planar PDMS adhesive (1.9 N m^{-1}) (Fig. 4C). This improvement primarily stems from the adaptability of the micropillar structures to rough surfaces (Fig. 4B and fig. S5). However, despite this improvement, the skin adhesion of MicroAdh remains much lower than that of Scotch tape. In addition, it lacks directional adhesion properties (Fig. 4D). In contrast, the metamaterial adhesives, although made of the same material as MicroAdh, exhibited higher adhesion strengths. The MetaAdh and MetaAdh-L demonstrated an adhesion strength of 39.0 and 54.7 N m^{-1}, respectively, on the skin in the maximum force direction (Fig. 4C). In the minimum force direction, the MetaAdh and MetaAdh-L showed an adhesion strength of 1.6 N m^{-1}, indicating substantial adhesion directionality of 23.7 to 32.3 (Fig. 4D). This highlights the effectiveness of the nonlinear cut-induced macroscale crack trapping, even on rough surfaces.

The hybrid film exhibited a remarkable increase in adhesion strength on rough skin surfaces. Specifically, the Hybrid-L displayed an adhesion strength of 110.9 N m^{-1} on porcine skin in the maximum peeling direction (Fig. 4C). Furthermore, the Hybrid-L maintained a consistently high adhesion strength of 83.9 N m^{-1} even on hairy porcine skin (fig. S6). This represents a substantial increase compared to flat PDMS (1.9 N m^{-1}), MicroAdh (4.5 N m^{-1}), and MetaAdh-L (54.7 N m^{-1}) adhesives, with enhancements of 58.4×, 24.6×, and 2.0×, respectively. The exceptional skin adhesion performance of the hybrid film arises from two main factors. First, the multiscale crack arresting effects enabled by the microscale pillar array and macroscale nonlinear cut architectures play a pivotal role. Second, the micropillars enhance surface adaptability on rough skin surfaces, effectively increasing the interfacial contact area. Demonstrating robust skin adhesion in the maximum force direction, the HybridAdh adheres strongly when attached to the forearm and peeled forward (Fig. 4Ei). While exhibiting strong adhesion in the maximum force direction, the HybridAdh can be effortlessly released in the minimum force direction (Fig. 4Eii), showing outstanding adhesion directionality, close to 20 (Fig. 4D). It is noteworthy that achieving a reversible skin adhesion strength of approximately 110.9 N m^{-1} alongside adhesion directionality exceeding 20 represents the highest and exceptional performance among previous reversible skin adhesives (Fig. 4F and table S1) (*49*–*56*).

Applications of the crack-trapping hybrid adhesive patch

The hybrid adhesive patch provides independent programmability of peel and pull-off adhesion strengths at any location on the adhesive patch by strategically combining macroscopic cuts and micropillars. This provides a unique multidirection adhesion programmability, pushing toward three-dimensional control of adhesion, through the ability to trap cracks for high capacity and facilitate crack propagation for easy release in the normal direction, with micropillars, and in multiple peeling directions, with metamaterial adhesive cuts. As a conceptual demonstration, we designed three types of circular skin adhesive patches with distinct cut designs—types I, II, and III (fig. S7). All patches feature micropillars without cut patterns in their central region (diameter, 24 mm) to securely adhere to the skin (Fig. 5Ai), while allowing for the integration of various electronic components on the backside of the central region. Each patch type uses a unique cut design. For instance, patch type I incorporated two circular rows of open rectangular cuts adjacent to the central micropillar area, designed to prevent delamination caused by the weight of integrated components. Next to the inner two rows of cuts, two additional circular rows of cuts in the opposite direction were introduced to prevent edge peeling during everyday use. The patches can be comfortably removed when necessary by applying a peeling force that exceeds their adhesion strength. Micropillars covered the entire patch to strengthen pull-off and peeling adhesion performance. Consequently, the circular patch is anticipated to exhibit high peeling resistance while enabling the integration of sizeable devices in its center through high resistance to normal separation for robust skin adhesion.

To validate this design, we measured the adhesion strength of an adhesive strip with a similar cut design to the circular patch type I

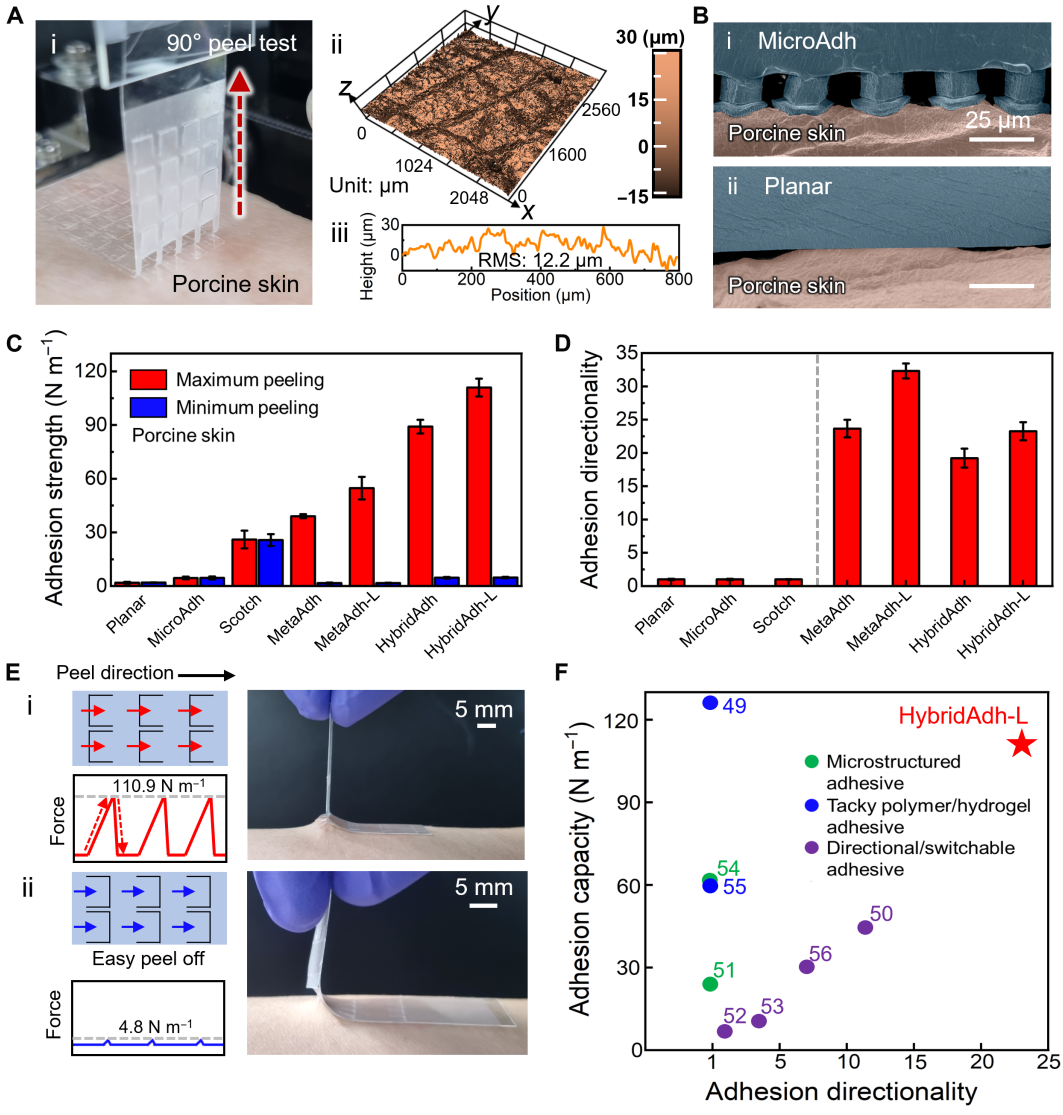

Fig. 4. Skin adhesion performance of the hybrid adhesive patch. (**A**) (i) Photograph depicting the 90° peel test of the hybrid adhesive (HybridAdh-L) on porcine skin. (ii) Confocal microscopy image displaying the surface morphology of porcine skin. (iii) Surface roughness of the porcine skin. (**B**) (i) SEM image showing the intimate contact between the hexagonal micropillars and porcine skin. (ii) SEM image showing the nonintimate contact between the planar adhesive and porcine skin. (**C**) Adhesion strengths measured for different adhesive samples against porcine skin (retraction rate, 1 mm s^{-1}). (**D**) Adhesion directionality of different adhesive samples on porcine skin. (**E**) Hybrid skin adhesive attached to the forearm subjected to (i) maximum force directional peeling and (ii) minimum force directional peeling. (**F**) Benchmark performance of skin adhesion for different reusable skin adhesives. More detailed information is available in table S1.

against porcine skin (Fig. 5A, ii to iv). During inward peeling (d_1 direction), substantial peel resistance was observed at c_1 (103.9 N m^{-1}) and c_2 (73.6 N m^{-1}). During outward peeling (d_2 direction), strong peel resistance with an adhesion strength of 70.5 N m^{-1} was observed at both c_3 and c_4 locations. These results confirm that the intended adhesive characteristics were well realized in the patch. The circular hybrid patch could firmly adhere to forearm skin while sustaining heavy objects (100 g) (Fig. 5B). Building upon the customized adhesive patch, we developed a wearable virtual reality (VR) avatar control device by integrating a battery, microcontroller unit (MCU), gyroscope sensor, and Bluetooth module on the upper part of the patch (Fig. 5C, i and ii). Despite its bulky size, the device securely adhered to the back of the hand and effectively captured human motion, wirelessly transmitting the data for real-time control of the avatar in VR applications. The smart adhesion properties of the patch can be customized by altering the cut design, as demonstrated with patch types II and III (fig. S7). For example, the type III hybrid patch, which consists of four circular rows of cuts all arranged in the same direction, exhibits unidirectional skin adhesion behavior (fig. S7Biii). This design allows for secure attachment of heavy and bulky devices while ensuring easier removal at a lower peeling force compared to types I or II.

In addition to its programmable adhesion capabilities, the hybrid adhesive patch showed excellent skin compatibility and breathability (fig. S8). Unlike commercial medical tape, which caused noticeable skin irritation after 3 days of attachment, our patch

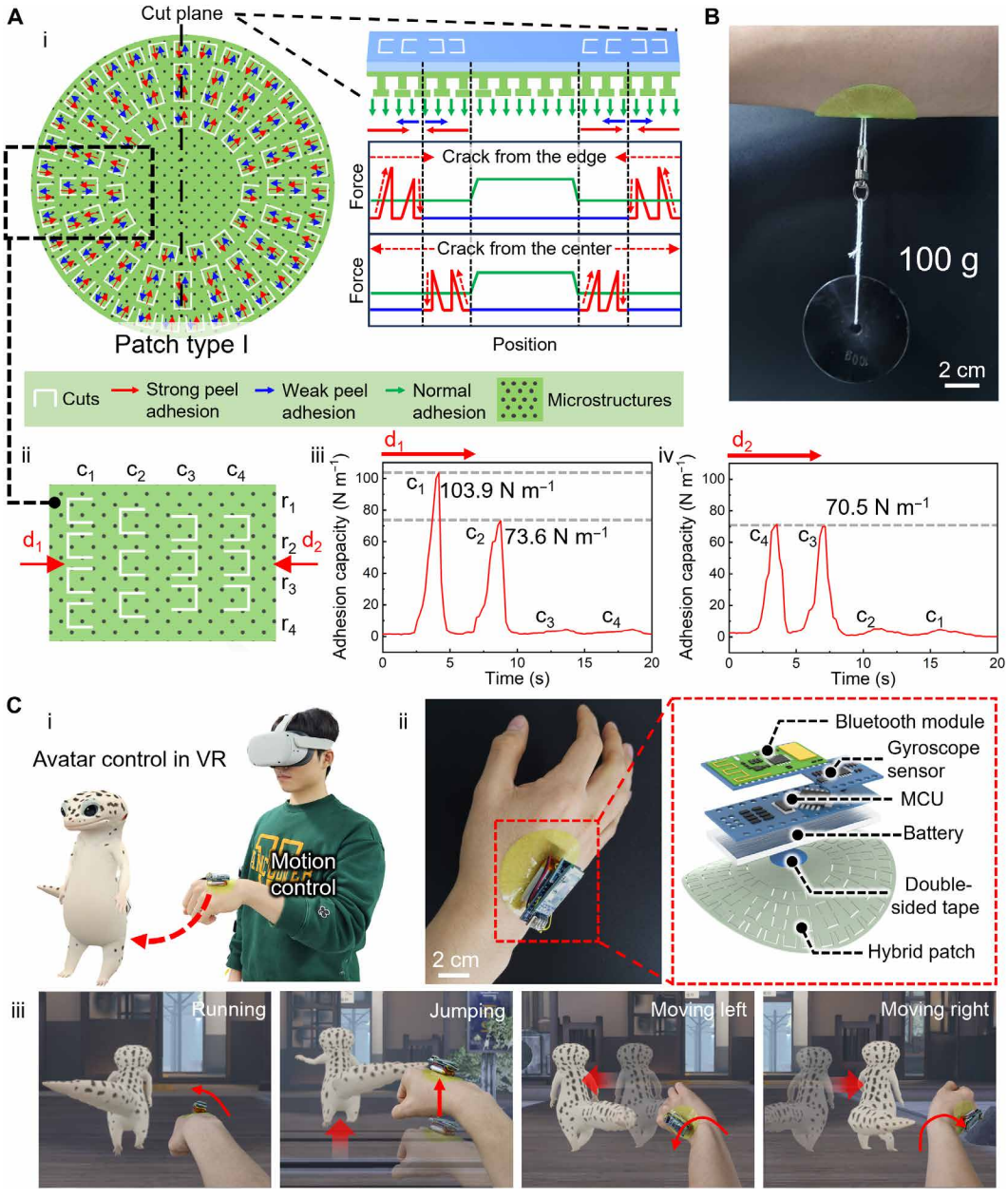

Fig. 5. Application of the hybrid adhesive patch. (**A**) (i) Design of the hybrid adhesive patch type I with programmed adhesion properties. (ii) Hybrid adhesive strip used for evaluating the adhesion properties of the patch type I. (iii) Measured adhesion strength of the patch during outward peeling (peeling along the d1 direction). (iv) Measured adhesion strength of the patch during inward peeling (peeling along the d2 direction). (**B**) Photograph demonstrating the patch's strong skin adhesion and its ability to withstand external loads. (**C**) (i) A device-integrated hybrid patch adhered to the back of a user's hand for VR applications. (ii) Photograph showing the hybrid patch integrated with battery, MCU, sensor, and Bluetooth module securely adhered to the back of the hand (total device weight, 20 g). (iii) Demonstration of the real-time avatar control in VR applications using the patch device.

caused no irritation. Moreover, it maintained high levels of peel adhesion capacity through 50 repeated attachment and detachment cycles, whereas the commercial tape rapidly lost its adhesion strength (fig. S9). This combination of long-term attachment, repeated adhesion capability, smart and programmable adhesion features, and the ability to integrate heavy and bulky electronics greatly enhances and expands the potential applications of various skin-mountable devices.

DISCUSSION

In summary, we have introduced a hybrid adhesive patch that effectively suppresses continuous crack propagation across bonded interfaces, spanning from micro to macroscales, through the integration of hexagonal micropillar arrays and engineered nonlinear cuts. Our strategy represents a robust methodology to regulate and program crack propagation across length scales, an approach that has been relatively unexplored until now. The multifunctional

hybrid adhesive patch demonstrated exceptional performance in various adhesion aspects: strong pull-off strength (272.7 kPa), high peel adhesion capacity (220.4 N m^{-1}), rough surface adaptability (skin adhesion of 110.9 N m^{-1}), high directionality (>20), and reusability (>50). These properties can be customized by adjusting the geometrical design and combining different microarchitectures and nonlinear cuts. For instance, micropillars with higher PSR can be used for moderate to lower pull-off adhesion. In addition, different types of nanoscale structures could be integrated with the micropillars and macroscale cut patterns to control interfacial cracks across more extended scales. Furthermore, instead of rectangular cuts, using rectangular cuts with triangular tips can enhance directionality (*38*). Nonlinear cuts of varying directions and sizes can also be selectively incorporated into the adhesive patch to program selective adhesion directionality and strength within a single adhesive patch. This enables the systematic and spatial control of adhesion in multiple directions across an adhesive film, providing pathways for fully programmable, multidirection adhesion control. The remarkable adhesion performance of the hybrid adhesive patch enabled the seamless integration of sizeable electronic components while providing robust skin adhesion, demonstrating its substantial utility for applications in wearable motion monitoring and VR interface devices. We anticipate that the multiscale crack-trapping adhesive patch will contribute to the advancement of smart adhesives, wearable devices, soft robotics, and intelligent manufacturing.

MATERIALS AND METHODS

Fabrication of the hybrid patch

The fabrication process began by creating a master mold featuring a negative pattern of hexagonal micropillars with mushroom-shaped tips on a Si wafer through photolithography (fig. S1). A lift-off resist (LOR 30 B, Microchem Corp., USA) and photoresist (SU-8 3010, Microchem Corp., USA) were sequentially spin coated onto a dehydrated Si wafer, forming a bilayer. Each spin-coating step was followed by a soft-baking process (30 min at 200°C for the LOR layer, 10 min at 95°C for the SU-8 layer). The negative micropillar pattern in the SU-8 layer was created through photomask-based selective ultraviolet exposure ($\lambda = 365$ nm, dose = 250 mJ cm^{-2}), followed by development using an SU-8 developer (Microchem Corp., USA) for 5 min. Subsequently, a LOR developer (AZ 400 K, AZ Electronics Materials Corp., USA) was used to selectively form a 4-μm-long undercut in the LOR layer. A PDMS prepolymer (Sylgard 184, Dow, USA) with a 5–wt % curing agent was then spin coated over the prepared master mold at 1000 rpm, followed by curing at 70°C for 1.5 hours in a convection oven. Next, a PET film (SKC, Republic of Korea) with a thin PDMS layer (PET thickness, 50 μm; spin-coated PDMS thickness, 75 μm) was prepared as the inextensible backing layer. The PDMS side of the PET backing film was bonded to the rear side of the replicated hexagonal micropillar array film using O_2 plasma–assisted bonding (treatment time, 3 min; power, 100 W; CUTE-1MPR, Femto Science, Republic of Korea). After bonding, the assembled micropillar-PET film was demolded from the master mold. Subsequently, open rectangular cuts were made in the assembled film, resulting in the creation of a micropillar-nonlinear cut hybrid adhesive patch. It is important to note that the master mold prepared can be used repeatedly (more than 100 times) for the replica molding process using PDMS, thereby reducing costs and fabrication times for intricate micropillar structures. The protruding tips of the molded PDMS could potentially lead to structural failures during the demolding process. However, the PDMS micropillars with protruding tips could be successfully demolded from the master mold without damage because of the high elasticity of PDMS. The ratio of tip thickness (2 to 3 μm) to protruding tip length (4 μm) ranges from 1.3 to 2 (*57*). Within this range, we did not observe any structural damage during demolding. However, if the ratio exceeds 3.5, the tip of the micropillars may be damaged during demolding (*57*). Even in cases of successful demolding, the tip part can still fold or collapse during attachment and detachment cycles.

Adhesion tests

The peel adhesion characteristics of the adhesive strips were assessed against glass or porcine skin substrates using a 90° peel test conducted on a Univert mechanical tester (Cellscale, Canada) (fig. S4). This test was carried out at a retraction rate of 1 mm s^{-1}. The substrates were affixed to a horizontally slidable sample holder using double-sided tape (3M, USA). Before each measurement, thorough cleaning of the adhesive strips and test substrates was performed using isopropyl alcohol. Subsequently, the adhesive strips were brought into contact with the substrates using a rubber roller. The critical energy release rates for both planar and microstructured PDMS films were determined using the same 90° peel test at a retraction rate of 1 mm s^{-1}. In addition, the normal adhesion strengths of the adhesive samples were measured using a custom-built adhesion tester comprising a substrate holder and a vertically movable jig (figs. S10 to S12). Adhesive samples were positioned on the horizontal surface of the jig, facing downwards. These adhesive samples were secured to the jig using grid-patterned double-sided adhesives (3M, USA) to ensure the nonlinear cuts' functionality (fig. S10). During the measurement, the adhesive samples were brought into contact with glass or porcine skin substrates, which were fixed on the substrate holder, with a controlled preload of 60 kPa. Subsequently, the sample-mounted jig was vertically moved upward until the samples detached from the substrates at a retraction rate of 1 mm s^{-1}. Throughout the test cycle, the adhesive forces were captured using a load cell (Ktoyo, Republic of Korea) connected to the jig of the equipment.

Surface analysis

SEM images of the hexagonal micropillars were acquired using an S-4800 microscope (Hitachi, Japan) following the sputtering of the microstructures with a 5-nm-thick Pt layer (K575X sputter, Quorum Emitech, UK). The surface topography of the porcine skin was assessed using a confocal microscope (LEXT OLS3100, Olympus, Japan). The roughness values roughness values were derived from the scanned images using LEXT OLS imaging analysis software.

Fabrication of the wireless motion monitoring device

The wireless motion control system was composed of an MCU (Arduino Nano Every; Arduino), a gyroscope sensor (SEN330201; YwRobot), a Bluetooth module (MD0269; KEYES), and a lithium-ion battery (3.7 V, 500 mAh, TW-902030; Thehan). The Bluetooth module, gyroscope sensor, and battery were soldered to the MCU, and the entire assembly was securely attached to the hybrid patch using double-sided tape. The hybrid patch, integrated with the motion control system, was then mounted on the back of the hand, allowing the gyro sensor to detect human motion. Operating on the principle of angular momentum, the gyro sensor captured changes in rotational

motion. The sensor's output was transmitted to the MCU. Subsequently, the MCU forwarded the sensor signals to another Bluetooth module connected to a computer, enabling users to control an avatar in a VR application.

Supplementary Materials

The PDF file includes:
Supplementary Notes S1 and S2
Tables S1 and S2
Figs. S1 to S12
Legend for movie S1

Other Supplementary Material for this manuscript includes the following:
Movie S1

REFERENCES AND NOTES

1. H. C. Ates, P. Q. Nguyen, L. Gonzalez-Macia, E. Morales-Narváz, F. Güder, J. J. Collins, C. Dincer, End-to-end design of wearable sensors. *Nat. Rev. Mater.* **7**, 887–907 (2022).
2. J. Park, H. W. Kim, S. Lim, H. Yi, Z. Y. Wu, I. G. Kwon, W.-H. Yeo, E. Song, K. J. Yu, Conformal fixation strategies and bioadhesives for soft bioelectronics. *Adv. Funct. Mater.* **34**, 2313728 (2024).
3. Y. Kim, G. A. Parada, S. Liu, X. Zhao, Ferromagnetic soft continuum robots. *Sci. Robot.* **4**, eaax7329 (2019).
4. S. Park, G. Choi, M. Kang, W. Kim, J. Kim, H. E. Jeong, Bioinspired magnetic cilia: From materials to applications. *Microsyst. Nanoeng.* **9**, 153 (2023).
5. W. Ruotolo, D. Brouwer, M. R. Cutkosky, From grasping to manipulation with gecko-inspired adhesives on a multifinger gripper. *Sci. Robot.* **6**, eabi9773 (2021).
6. C. Linghu, S. Zhang, C. Wang, K. Yu, C. Li, Y. Zeng, H. Zhu, X. Jin, Z. You, J. Song, Universal SMP gripper with massive and selective capabilities for multiscaled, arbitrarily shaped objects. *Sci. Adv.* **6**, eaay5120 (2020).
7. D. Wang, H. Hu, S. Li, H. Tian, W. Fan, X. Li, X. Chen, A. C. Taylor, J. Shao, Sensing-triggered stiffness-tunable smart adhesives. *Sci. Adv.* **9**, eadf4051 (2023).
8. D. J. Levine, O. A. Lee, G. M. Campbell, M. K. Mcbride, H. J. Kim, K. T. Turner, R. C. Hayward, J. H. Pikul, A low-voltage, high-force capacity electroadhesive clutch based on ionoelastomer heterojunctions. *Adv. Mater.* **35**, 2304455 (2023).
9. Z.-H. Wang, B.-W. Liu, F.-R. Zeng, X.-C. Lin, J.-Y. Zhang, X.-L. Wang, Y.-Z. Wang, H.-B. Zhao, Fully recyclable multifunctional adhesive with high durability, transparency, flame retardancy, and harsh- environment resistance. *Sci. Adv.* **8**, eadd8527 (2022).
10. H. Ren, Z. Zhang, X. Cheng, Z. Zou, X. Chen, C. He, Injectable, self-healing hydrogel adhesives with firm tissue adhesion and on-demand biodegradation for sutureless wound closure. *Sci. Adv.* **9**, eadh4327 (2023).
11. S.-H. Byun, J. Y. Sim, Z. Zhou, J. Lee, R. Qazi, M. C. Walicki, K. E. Parker, M. P. Haney, S. H. Choi, A. Shon, G. B. Gereau, J. Bilbily, S. Li, Y. Liu, W.-H. Yeo, J. G. McCall, J. Xiao, J.-W. Jeong, Mechanically transformative electronics, sensors, and implantable devices. *Sci. Adv.* **5**, eaay0418 (2019).
12. J. Li, A. D. Celiz, J. Yang, Q. Yang, I. Wamala, W. Whyte, B. R. Seo, N. V. Vasilyev, J. J. Vlassak, Z. Suo, D. J. Mooney, Tough adhesives for diverse wet surfaces. *Science* **357**, 378–381 (2017).
13. D. Kim, J. Lee, M. K. Park, S. H. Ko, Recent developments in wearable breath sensors for healthcare monitoring. *Commun. Mater.* **5**, 41 (2024).
14. S. Kondaveeti, G. Choi, S. C. Veerla, S. Kim, J. Kim, H. J. Lee, U. Kuzhiumparambil, P. J. Ralph, J. Y. Yeo, H. E. Jeong, Mussel-inspired resilient hydrogels with strong skin adhesion and high-sensitivity for wearable device. *Nano Converg.* **11**, 12 (2024).
15. Q. Yang, Z. Hu, J. A. Rogers, Functional hydrogel interface materials for advanced bioelectronic devices. *Acc. Mater. Res.* **2**, 1010–1023 (2021).
16. H.-C. Liu, Y. Zeng, C. Gong, X. Chen, P. Kijanka, J. Zhang, Y. Genyk, H. Tchelepi, C. Wang, Q. Zhou, X. Zhao, Wearable bioadhesive ultrasound shear wave elastography. *Sci. Adv.* **10**, eadk8426 (2024).
17. Y. Zhang, S. Ma, B. Li, B. Yu, H. Lee, M. Cai, S. N. Gorb, F. Zhou, W. Liu, Gecko's feet-inspired self-peeling switchable dry/wet adhesive. *Chem. Mater.* **33**, 2785–2795 (2021).
18. K. Mendez, W. Whyte, B. R. Freedman, Y. Fan, C. E. Varela, M. Singh, J. C. Cintron-Cruz, S. E. Rothenbücher, J. Li, D. J. Mooney, E. T. Roche, Mechanoresponsive drug release from a flexible, tissue-adherent, hybrid hydrogel actuator. *Adv. Mater.* **2023**, 2303301 (2023).
19. H. J. Lee, H. Kim, T. S. Kim, H. Y. Kim, J. Mun, G. Choi, H. E. Jeong, J. Yeo, Adhesive-free PDMS/PUA bilayer using selective photopolymerization for transparent, attachable, and wearable triboelectric nanogenerator. *Nano Energy* **121**, 109274 (2024).
20. J. Ok, S. Park, Y. H. Jung, T.-I. Kim, Wearable and implantable cortisol-sensing electronics for stress monitoring. *Adv. Mater.* **36**, 2211595 (2024).
21. G. Wan, W. Shan, Pneumatically tunable adherence of elastomeric soft hollow pillars with non-circular contacts. *Int. J. Solids Struct.* **294**, 112736 (2024).
22. J. Cui, D.-M. Drotlef, I. Larraza, J. P. Fernández-Blázquez, L. F. Boesel, C. Ohm, M. Mezger, R. Zentel, A. del Campo, Bioinspired actuated adhesive patterns of liquid crystalline elastomers. *Adv. Mater.* **24**, 4601–4604 (2012).
23. J. Shim, S.-H. Bae, W. Kong, D. Lee, K. Qiao, D. Nezich, Y. J. Park, R. Zhao, S. Sundaram, X. Li, H. Yeon, C. Choi, H. Kum, R. Yue, G. Zhou, Y. Ou, K. Lee, J. Moodera, X. Zhao, J.-H. Ahn, C. Hinkle, A. Ougazzaden, J. Kim, Controlled crack propagation for atomic precision handling of wafer-scale two-dimensional materials. *Science* **362**, 665–670 (2018).
24. G. Wan, Y. Tang, K. T. Turner, T. Zhang, W. Shan, Tunable dry adhesion of soft hollow pillars through sidewall buckling under low pressure. *Adv. Funct. Mater.* **33**, 2209905 (2023).
25. E. M. Thomas, H. Fu, R. C. Hayward, A. J. Crosby, Geometry-controlled instabilities for soft-soft adhesive interfaces. *Soft Matter* **18**, 8098–8105 (2022).
26. N. J. Glassmaker, A. Jagota, C. Y. Hui, W. L. Noderer, M. K. Chaudhury, Biologically inspired crack trapping for enhanced adhesion. *Proc. Natl. Acad. Sci. U.S.A.* **104**, 10786–10791 (2007).
27. E. Kizilkan, S. N. Gorb, Combined effect of the microstructure and underlying surface curvature on the performance of biomimetic adhesives. *Adv. Mater.* **30**, 1704696 (2018).
28. M. Samri, J. Thiemecke, E. Prinz, T. Dahmen, R. Hensel, E. Arzt, Predicting the adhesion strength of micropatterned surfaces using supervised machine learning. *Mater Today* **53**, 41–50 (2022).
29. M. N. Khan, T. Huo, Q. Zhang, Z. Hu, J. Zhao, J. Chen, Z. Wang, K. Ji, Synergetic adhesion in highly adaptable bio-inspired adhesive. *Colloid Surface B Biointerfaces* **212**, 112335 (2022).
30. H. Zhao, J. J. Wie, D. Copic, C. R. Oliver, A. O. White, S. Kim, A. J. Hart, High-fidelity replica molding of glassy liquid crystalline polymer microstructures. *ACS Appl. Mater. Interfaces* **8**, 8110–8117 (2016).
31. C.-Y. Hui, R. Long, K. J. Wahl, R. K. Everett, Barnacles resist removal by crack trapping. *J. R. Soc. Interface* **8**, 868–879 (2011).
32. A. B. Croll, N. Hosseini, M. D. Bartlett, Switchable adhesives for multifunctional interfaces. *Adv. Mater. Technol.* **4**, 1900193 (2019).
33. C. B. Haverkamp, D. Hwang, C. Lee, M. D. Bartlett, Deterministic control of adhesive crack propagation through jamming based switchable adhesives. *Soft Matter* **17**, 1731–1737 (2021).
34. K. Kendall, Control of cracks by interfaces in composites. *Proc. R. Soc. Lond. A Math. Phys. Sci.* **341**, 409–428 (1975).
35. D.-G. Hwang, K. Trent, M. D. Bartlett, Kirigami-inspired structures for smart adhesion. *ACS Appl. Mater. Interfaces* **10**, 6747–6754 (2018).
36. R. Zhao, S. Lin, H. Yuk, X. Zhao, Kirigami enhances film adhesion. *Soft Matter* **14**, 2515–2525 (2018).
37. P. Won, J. J. Park, T. Lee, I. Ha, S. Han, M. Choi, J. Lee, S. Hong, K.-J. Cho, S. H. Ko, Stretchable and transparent kirigami conductor of nanowire percolation network for electronic skin applications. *Nano Lett.* **19**, 6087–6096 (2019).
38. D. Hwang, C. Lee, X. Yang, J. M. Pérez-González, J. Finnegan, B. Lee, E. J. Markvicka, R. Long, M. D. Bartlett, Metamaterial adhesives for programmable adhesion through reverse crack propagation. *Nat. Mater.* **22**, 1030–1038 (2023).
39. Y. Tang, G. Lin, S. Yang, Y. K. Yi, R. D. Kamien, J. Yin, Programmable kiri-kirigami metamaterials. *Adv. Mater.* **29**, 1604262 (2017).
40. S. Xia, L. Ponson, G. Ravichandran, K. Bhattacharya, Toughening and asymmetry in peeling of heterogeneous adhesives. *Phys. Rev. Lett.* **108**, 196101 (2012).
41. M. C. Bélanger, Y. Marois, Hemocompatibility, biocompatibility, inflammatory and studies of primary reference materials low-density polyethylene and polydimethylsiloxane: A review. *J. Biomed. Mater. Res.* **58**, 467–477 (2001).
42. I. Miranda, A. Souza, P. Sousa, J. Ribeiro, E. M. S. Castanheira, R. Lima, G. Minas, Properties and applications of PDMS for biomedical engineering: A review. *J. Funct. Biomater.* **13**, 2 (2022).
43. I. Hwang, M. Seong, H. Yi, H. Ko, H.-H. Park, J. Yeo, W.-G. Bae, H. W. Park, H. E. Jeong, Low-resistant electrical and robust mechanical contacts of self-attachable flexible transparent electrodes with patternable circuits. *Adv. Funct. Mater.* **30**, 2000458 (2020).
44. K. Jin, Y. Tian, J. S. Erickson, J. Puthoff, K. Autumn, N. S. Pesika, Design and fabrication of gecko-inspired adhesives. *Langmuir* **28**, 5737–5742 (2012).
45. S. Kim, M. Sitti, T. Xie, X. Xia, Reversible dry micro-fibrillar adhesives with thermally controllable adhesion. *Soft Matter* **5**, 3689–3693 (2009).
46. M. D. Bartlett, S. W. Case, A. J. Kinloch, D. A. Dillard, Peel tests for quantifying adhesion and toughness: A review. *Prog. Mater. Sci.* **137**, 101086 (2023).
47. K. Kendall, Thin-film peeling-the elastic term. *J. Phys. D Appl. Phys.* **8**, 1449–1452 (1975).
48. Q. Li, W. Liu, C. Yang, P. Rao, P. Lv, H. Duan, W. Hong, Kirigami-inspired adhesion with high directional asymmetry. *J. Mech. Phys. Solids* **169**, 105053 (2022).
49. S. Baik, J. Kim, H. J. Lee, T. H. Lee, C. Pang, Highly adaptable and biocompatible octopus-like adhesive patches with meniscus-controlled unfoldable 3D microtips for underwater surface and hairy skin. *Adv. Sci.* **5**, 1800100 (2018).

50. M. Gao, H. Wu, R. Plamthottam, Z. Xie, Y. Liu, J. Hu, S. Wu, L. Wu, X. He, Q. Pei, Skin temperature-triggered, debonding-on-demand sticker for a self-powered mechanosensitive communication system. *Matter* **4**, 1962–1974 (2021).
51. Z. Gu, X. Wan, Z. Lou, F. Zhang, L. Shi, S. Li, B. Dai, G. Shen, S. Wang, Skin adhesives with controlled adhesion by polymer chain mobility. *ACS Appl. Mater. Interfaces* **11**, 1496–1502 (2019).
52. Y. Jiang, X. Zhang, W. Zhang, M. Wang, L. Yan, K. Wang, L. Han, X. Lu, Infant skin friendly adhesive hydrogel patch activated at body temperature for bioelectronics securing and diabetic wound healing. *ACS Nano* **16**, 8662–8676 (2022).
53. K. R. Jinkins, S. Li, H. Arafa, H. Jeong, Y. J. Lee, C. Wu, E. Campisi, X. Ni, D. Cho, Y. Huang, J. A. Rogers, Thermally switchable, crystallizable oil and silicone composite adhesives for skin-interfaced wearable devices. *Sci. Adv.* **8**, eabo0537 (2022).
54. J. Lee, B. S. Lee, S. Baik, D. W. Kim, N.-J. Park, J. W. Lee, S.-K. Bong, S. H. Lee, S.-N. Kim, J. H. Song, J. K. Kim, G.-R. Yi, K. H. Kim, C. Pang, Ultra-intimate hydrogel hybrid skin patch with asymmetric elastomeric spatula-like cylinders. *Chem. Eng. J.* **444**, 136581 (2022).
55. S. Wang, Y. Fang, H. He, L. Zhang, C. Li, J. Ouyang, Wearable stretchable dry and self-adhesive strain sensors with conformal contact to skin for high-quality motion monitoring. *Adv. Funct. Mater.* **31**, 2007495 (2021).
56. H. Yi, S.-H. Lee, H. Ko, D. Lee, W.-G. Bae, T. Kim, D. S. Hwang, H. E. Jeong, Ultra-adaptable and wearable photonic skin based on a shape-memory, responsive cellulose derivative. *Adv. Funct. Mater.* **29**, 1902720 (2019).
57. H. Yi, M. Kang, M. K. Kwak, H. E. Jeong, Simple and reliable fabrication of bioinspired mushroom-shaped micropillars with precisely controlled tip geometries. *ACS Appl. Mater. Interfaces* **8**, 22671–22678 (2016).

Acknowledgments

Funding: This work was supported by the National Research Foundation of Korea grant funded by the Korea government (MSIT) (NRF-2021R1A2C3006297 and RS-2024-00432685). C.L. and M.D.B. acknowledge support from the National Science Foundation under the DMREF program (award number 2119105). **Author contributions:** S.P., D.K.K., and D.L. performed the experiments and wrote the manuscript. G.C. and J.K. assisted with the experiments. C.L. analyzed the experimental results and reviewed the manuscript. M.S. consulted on the experiments, analyzed the experimental results, and reviewed the manuscript. M.D.B. consulted on the experiments, analyzed the experimental results, and wrote the manuscript. H.E.J. conceived and supervised the research and also wrote the manuscript. **Competing interests:** The authors declare that they have no competing interests. **Data and materials availability:** All data needed to evaluate the conclusions in the paper are present in the paper and/or the Supplementary Materials.

Submitted 20 May 2024
Accepted 6 August 2024
Published 11 September 2024
10.1126/sciadv.adq3438